IEEE Access
Multidisciplinary | Rapid Review | Open Access Journal

Received June 3, 2019, accepted June 30, 2019, date of publication July 15, 2019, date of current version August 8, 2019.

Digital Object Identifier 10.1109/ACCESS.2019.2929003

Pulse-Compression Signal Propagation and Parameter Estimation in the Troposphere With Parabolic Equation

DONGMIN ZHANG, CHENG LIAO, JU FENG, AND XIAOCHUAN DENG
Institute of Electromagnetic, Southwest Jiaotong University, Chengdu 610031, China

Corresponding author: Cheng Liao (c.liao@swjtu.edu.cn)

This work was supported in part by the National Natural Science Foundation of China under Grant 61771407, and in part by the National Science Foundation for Young Scientists of China under Grant 61801405.

ABSTRACT Wireless channel analysis is essential in the design, performance evaluation, and error correction of radar system. In this paper, an efficient parabolic equation (PE) method, which employs the split-step Fourier transform (SSFT) solution and Fourier synthesis technique, is developed for the propagation and parameter estimation of pulse-compression signals in the troposphere considering anomalous propagation conditions. A sliding window method is applied to reduce computational loads for long-distance propagation in time-domain PE. The signal delay is obtained via searching the peak of the correlation function of the received signal and a known reference signal according to the autocorrelation of the signals. The numerical examples indicate that the presented method is well suited for pulse-compression signals. Beyond that, a multiple signal classification (MUSIC) algorithm with spatial smoothing technique is introduced to obtain the signal direction of arrival (DOA) in PE model, where the covariance matrix is constructed via the array fields obtained from PE and the curvature of wavefronts due to the atmospheric refraction is considered in the array steering vector. The numerical examples verify the accuracy of the presented method. The simulation experiments in a typical sea-to-land scenario are presented to analyze the sensitivity of pulse-compression signals to evaporation ducts, including pulse waveform, time delay, and DOA, utilizing the presented methods.

INDEX TERMS Parabolic equation (PE), troposphere, radio wave propagation, pulse-compression signal, parameter estimation.

I. INTRODUCTION

The pulse-compression signals, such as the linear frequency modulation (LFM) signals, non-linear frequency modulation (NLFM) signals, and phase coded signals (PCSs), which have large time-bandwidth product, are commonly used in modern radar system. In the pulse compression process, the impulse response function of the matched filter is designed to be a conjugate mirror of the transmitted signal to get the best signal-to-noise ratio (SNR) for signal detection. In practice, the propagation of radar signal in the troposphere is often influenced by atmospheric, irregular terrains, ground vegetation, sea clutter, and so on [1]–[5], resulting in signal attenuation, distortion, additional delay, and propagation direction change. In particular, atmospheric refraction reduces the precision of target orientation in radar system because of the estimation errors of elevation angle and propagation delay, as shown in Fig.1.

Electromagnetic wave propagation in a realistic environment is very complicated, so effective methods are required to analyze the wireless channel in radar system design. The full-wave methods provide accuracy solutions, such as the finite difference time domain (FDTD) method [6], [7] and the method of moment (MOM) [8], but these methods confront heavy burden from a huge number of unknown variables in the microwave band. The radar equation has the merits of simplicity and fast calculation, but it is insufficient to provide a full consideration of the realistic environment and fails to implement signal parameter estimation. The parabolic equation (PE) is an approximation of Helmholtz equation [9]. It takes the influences of various environmental factors into account,

The associate editor coordinating the review of this manuscript and approving it for publication was Mohammed Bait Suwailam.

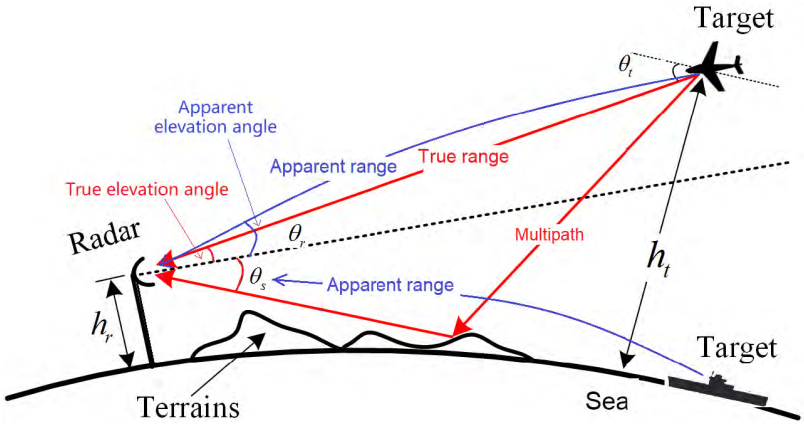

FIGURE 1. Angle and range estimation errors due to atmospheric refraction.

such as the atmospheric conditions [10], [11], irregular terrains [12], [13], vegetation [14], [15], buildings [16], and rainfall [17], and has a remarkable advantage in computational efficiency with the split-step Fourier transform (SSFT) solution [18], so it is especially suitable for large-range propagation problems. There have been considerable research efforts to deal with the radio wave propagation problem in the troposphere with PE method [10]–[17]. However, most of the studies were concerned with the frequency-domain representation, in which the parameters evaluated are mainly field strength, propagation factor, or path loss.

For a comprehensive wireless channel estimation, the time domain approach becomes a better choice. The Fourier synthesis technique can be adopted to convert the original PE to a time-domain version (TD-PE) for pulse propagation problems [19]. However, because of the periodicity of Fourier transforms in the time-frequency conversion, the time-domain observation window is usually required to be set large enough to avoid time folding phenomenon, resulting in enormous calculations for long-distance propagations. Beyond that, in a realistic scenario, the attenuation, multi-path effects, clutters and receiver thermal noise may lead to signal distortions and fading, making it difficult to obtain the signal delay from TD-PE directly.

Direction of arrival (DOA) is another signal characteristic parameter concerned in radar system besides time delay [20]–[22], which helps to quickly determine the locations of radiation sources or targets. A plane wave spectral (PWS) method [23] was used to obtain the DOA information in PE, which assumes that the refractivity is constant. When the approximation of a constant refractivity fails (in lager gradient refractivity cases, e.g., in the duct environments), the PWS method is no longer applicable. Ali Karimian [24] proposed a curved wave spectral (CWS) method that considers the curvature of waveforms due to the change of refractivity and can be applied to any atmospheric conditions, but a large synthetic aperture is required to retain precision.

In this paper, the PE method is developed to model the propagation of pulse-compression signals in the troposphere and to estimate the characteristic parameters of the signals. A sliding window method is used to reduce the length of the observation window by amplitude-phase separation. The delay of the signal is extracted by a peak search of the correlation function of the received signal and a reference signal. Numerical examples show that this method is well suited for pulse-compression signals. In addition, a multiple signal classification (MUSIC) algorithm [22] which provides a higher resolution compared with the traditional wave spectral methods is introduced to obtain the DOAs of the signals, where the covariance matrix is constructed via the array fields obtained from PE and the curvature of wavefronts due to the atmospheric refraction is considered in the array steering vector. Numerical examples are presented to verify the correctness and effectiveness of this method. Finally, with the presented methods, experiments are carried out to analyze the sensitivity of pulse-compression signals to atmospheric ducts in a typical sea-to-land scenario.

This paper is organized as follows. Section II outlines PE and its time-domain solution, the time-delay and DOA estimation methods in PE. Validations and discussions about the presented methods are provided in Section III. Simulation experiments in a sea-to-land environment are presented in Section IV. The Section V concludes the whole paper.

II. METHODS AND FORMULATIONS

A. PE WITH SSFT SOLUTION

The parabolic equation is an approximation of the Helmholtz equation with the neglect of backscattering. In Cartesian coordinates, assume the time-dependence of electromagnetic wave is $e^{j\omega t}$, the reduced function obtained from the electromagnetic field component via eliminating the fast varying phase term in the x direction, is given by

$$u(x, z) = e^{jk_0 x}\phi(x, z), \tag{1}$$

where x is the horizontal range, z is the altitude, and k_0 is the wavenumber in free space. $\phi = E_y$ for horizontal polarization and $\phi = H_y$ for vertical polarization, respectively.

Then, the PE of Feit-Fleck type derived from the Helmholtz equation is expressed as [9]

$$\frac{\partial u}{\partial x} = -j\left\{\sqrt{k_0^2 + \frac{\partial^2}{\partial z^2}} + k_0\left[n(x,z) - 2\right]\right\}u, \tag{2}$$

where n is the refractive index of the propagation medium.

By introducing the well-known split-step Fourier transform (SSFT) algorithm [18], the solution to (2) is given by

$$u(x+\Delta x, z) = \Im^{-1}\left\{e^{-j\sqrt{k_0^2 - k_z^2}^{*}\Delta x}\Im\left[e^{-jk_0\Delta x(n-2)}u(x,z)\right]\right\}. \tag{3}$$

where the operators $\Im$ and $\Im^{-1}$ represent the fast Fourier transforms (FFT) and the inverse transforms (IFFT), respectively. The symbol $*$ denotes the conjugation. Herein Δx is the step size along the propagation axis (x-axis). The transform variable $k_z = k_0 sin\theta$, where θ is the angle from the horizon.

using (3), the field distribution in the whole computational region can be solved via a step-by-step iterative approach when the initial field is provided. Both impedance boundary condition [25] and the conformal mapping methods [26] can be employed to describe ground effects, and a Hamming window is usually applied to truncate the upper boundary.

B. TIME-DOMAIN COUNTERPART OF PE

The PE presented above is essentially a frequency domain method. The Fourier synthesis is employed to solve the problems of pulse signal propagation, giving by

$$\phi(x,z,t) = \int_{-\infty}^{\infty} H(f)\phi(x,z,f)e^{j2\pi ft}df, \tag{4}$$

where $\phi(x,z,f)$ is the electromagnetic field at position (x,z) calculated by PE in the frequency domain, and $H(f)$ is the spectrum function of the transmitted signal.

The fast Fourier transform technique is applied to solve (4). According to the sampling theorem, the time interval Δt and frequency interval Δf should satisfy $\Delta t \cdot \Delta f = 1/N$, where N is the sampling number. The number of frequency points involved in PE calculation is $N_f = B \cdot T_w$, where B is the signal bandwidth and $T_w = N \cdot \Delta t$ is the length of time-domain observation window.

Due to the periodicity of Fourier transforms in the time-frequency conversion, T_w is required to be large enough to avoid time folding phenomenon. Since the frequency interval ($\Delta f = 1/T_w$) decreases with T_w, there would be a sharp increase in the number of frequency points in PE calculation when dealing with the long-distance propagation. In this paper, this problem is effectively mitigated via a sliding window approach, in which the reduced function u instead of ϕ is applied to time-frequency conversion. Correspondingly, (4) is rewritten as

$$u(x,z,t) = \int_{-\infty}^{\infty} H(f)u(x,z,f)e^{j2\pi ft}df. \tag{5}$$

Since $u(f)$ eliminates the phase term in the x direction, the delay in (5) becomes

$$\tau_u = \tau_r - x/c_0, \tag{6}$$

where τ_r is the actual delay of concern, and $c_0 = 3\times 10^8\ m/s$ is the electromagnetic wave speed in free space. Since $\tau_u > 0$ holds in practice, we get

$$\frac{x}{c_0} < \tau_r < T_w = \frac{x}{c_0} + T_w', \tag{7}$$

where T_w' is the length of the sliding window. Thus, the sampling number required to be calculated in frequency-domain PE becomes $N_f' = B \cdot T_w'$. In a long-distance propagation case, there is $N_f' \ll N_f$ thanks to $T_w' \ll T_w$. Correspondingly, the computational cost is reduced by $\frac{N_f - N_f'}{N_f}\%$.

C. TIME-DELAY ESTIMATION IN PE

The pulse waveform can be obtained directly using (3) and (5) with the consideration of the environmental disturbances, but the delay τ_r fails to be provided directly. In this paper, in order to obtain τ_r in a complex propagation environment, a cross-correlation operation between the received signal and a known reference signal is used to extract the relative delay of this two signals firstly.

The cross-correlation function of the received signal $S_r(t)$ and reference signal $S_{ref}(t)$ is defined as

$$R(t) = \Im^{-1}\{\Im[S_r(t)] \times \Im^{*}[S_{ref}(t)]\}, \tag{8}$$

where the operators $\Im$ and $\Im^{-1}$ represent the fast Fourier transforms (FFT) and its inverse transforms (IFFT), respectively. The symbol $*$ denotes the conjugation.

Considering the framework of time-domain PE presented above, we chose $S_{ref}(t) = u(x_t, z_t, t)$ and $S_r(t) = u(x_r, z_r, t)$, where the subscripts t and r denote the transmitting and receiving antennas, respectively.

With a peak search, the time t corresponding to the maximum value of $R(t)$ is given by

$$\tau_{add} = argmax\{R(t)\}. \tag{9}$$

According to the definition of $R(t)$, τ_{add} is a relative delay between $S_r(t)$ and $S_{ref}(t)$. Apparently, there is $\tau_{add} = \tau_u$.

The actual delay of the received signal is then obtained according to (6)

$$\tau_r = \tau_{add} + \frac{|x_r - x_t|}{c_0}, \tag{10}$$

where $|x_r - x_t|$ is the projection distance between the transmitting and receiving antennas.

It can be seen that the process of the time delay estimation presented above is essentially consistent with that of the pulse compression in radar system. Accordingly, this method is especially suitable for the pulse compression signals, such as the LFM signals and PCSs.

D. DOA ESTIMATION IN PE

Assume a uniform linear array (ULA) with M elements is located at position $p(x_r, h_r)$ in the computational region of PE, as depicted in Fig.2, the electromagnetic field impinged on the array can be expressed as $\phi[x_r, (m-1)\Delta z], m = 1, 2, \ldots, M$, where m is the serial number of the array elements and Δz is the inter-element spacing. Since $p(x_r, h_r)$ is far from the signal source, the field amplitudes on the elements are approximately equal, while the phases show difference and are related to the wavefront. Through utilizing the geometric relations, the phase difference between ϕ_m and ϕ_1 can be expressed [24]

$$\varphi_m(\theta) = \int_{z_1}^{z_m} k_v(z, \theta) dz, \tag{11}$$

where θ is the incident angle and k_v is the vertical wavenumber.

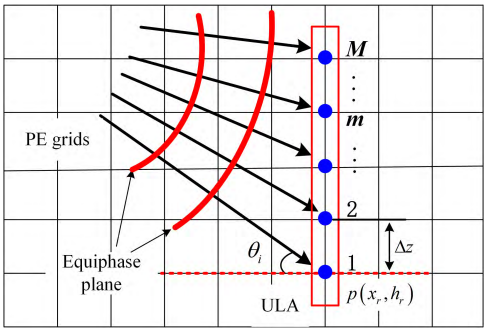

FIGURE 2. A sketch map of DOA estimation in parabolic equation.

According to the Snell's law, the horizontal wavenumber k_h is constant, yielding

$$\begin{aligned} k_v(z, \theta) &= \sqrt{k^2(z) - k_h^2(z, \theta)} \\ &= \frac{2\pi}{\lambda}\sqrt{n_r^2(z) - n_r^2(z_1)cos^2\theta}, \end{aligned} \tag{12}$$

where λ is wavelength in free space, n_r is the modified refractive index, and z_1 is the height of the reference element.

A array steering vector corresponding to the direction θ is defined as

$$\boldsymbol{a}(\theta) = \left[e^{-j\varphi_1(\theta)}, e^{-j\varphi_2(\theta)}, \cdots, e^{-j\varphi_M(\theta)}\right]^T, \tag{13}$$

where $(\cdot)^T$ denotes the transpose.

Note that (13) is a general expression which can be applied to any atmospheric refractive index profile. Assuming a constant refractivity, the phase difference between the first and the mth elements can be expressed as

$$\varphi_m = \frac{2\pi}{\lambda}\Delta z(m-1)sin\theta, \tag{14}$$

Correspondingly, the array steering vector is rewritten as

$$\boldsymbol{a}(\theta) = \left[1, e^{-j\frac{2\pi}{\lambda}\Delta zsin\theta}, \cdots, e^{-j\frac{2\pi}{\lambda}(M-1)\Delta zsin\theta}\right]^T, \tag{15}$$

The fundamental framework of the MUSIC algorithm is eigenvalue decomposition of array covariance matrix. Here, the array covariance matrix constructed by PE is given by

$$\hat{A}_{MM} = \phi[x_r, (m-1)\Delta z] \times \phi[x_r, (m-1)\Delta z]^H, \tag{16}$$

where $(\cdot)^H$ represents the conjugate transpose.

Performing eigenvalue decomposition on $\hat{A}_{MM}$, produces M eigenvalues and eigenvectors, where the D eigenvectors corresponding to the large eigenvalues are related to the arriving waves, while the others are only related to noise. Hence, we can divide the eigenvectors into two orthogonal subspaces, i.e. signal subspace $\boldsymbol{E}_s$ and noise subspace $\boldsymbol{E}_n$, respectively.

$$\begin{cases} \boldsymbol{E}_s = \{V_1, V_2, \ldots, V_D\}, & \rho_1 > \rho_2 > \cdots > \rho_D \\ \boldsymbol{E}_n = \{V_{D+1}, V_{D+2}, \cdots, V_M\} & \rho_{D+1} > \cdots > \rho_M \approx 0 \end{cases} \tag{17}$$

where V_m and ρ_m represent the eigenvector and the corresponding eigenvalue.

Since the noise subspace $\boldsymbol{E}_n$ and the steering vector $\boldsymbol{a}(\theta)$ are orthogonal in the direction of θ, the objective function can be defined as [22]

$$J(\theta) = \frac{\|\boldsymbol{a}(\theta)\|_2}{|\boldsymbol{a}^H(\theta)\boldsymbol{E}_n\boldsymbol{E}_n^H\boldsymbol{a}(\theta)|}, \tag{18}$$

where $\|\cdot\|_2$ represents the l_2 norm of a vector. When $\|\boldsymbol{a}(\theta)\boldsymbol{E}_n\|_2 = 0$ holds, the objective function results in a peak in the direction of θ. The DOA information of the signal can be obtained via a peak search. In practical applications, the signal subspace may diffuse into the noise subspace because of the highly correlated nature of the direct and multi-path waves, which results in a degraded estimation accuracy. A forward/backward spatial smoothing technique was proposed to solve this problem via decomposing the array into multiple overlapping sub-arrays, which is elaborated in details in reference [27].

III. EXAMPLES AND DISCUSSION

A. PLUSE-COMPRESSION SIGNALS

Both long range (a wide pulse width is required) and high resolution (a narrow pulse width is required) are usually expected in radar system, such as the surveillance radars and tracing radars. The pulse compression technique has been proved to be an pretty effective solution to alleviate the contradiction between the long-range and high-resolution. The linear frequency modulation signals are commonly employed in the pulse compression radar system, giving by

$$S_{lfm}(t) = A \cdot rect(\frac{t}{T})e^{j2\pi(f_c t + \frac{1}{2}\mu t^2)}, \quad -\frac{T}{2} \le t \le \frac{T}{2} \tag{19}$$

where $rect(\cdot)$ represents the rectangular envelope, A is the amplitude of the signal, and f_c is the center frequency of the signal. $\mu = B/T$ is the slope of the frequency modulation with bandwidth B and pulse duration T. Fig.3(a) shows the

waveform and spectrum of a LFM signal with $A = 1$ V/m, $T = 1$ us, $B = 20$ MHz and $f_c = 25$ MHz.

Beyond LFM signal, the phase coded signals (PCSs) such as the Barker code signal and Frank code signal, with the merits of information hiding, low probability of intercept and anti-jamming, are also widely adopted, which can be expressed as

$$S_{pcs}(t) = \sum_{n=1}^{N} q(t - nT_d)e^{j(2\pi f_c t + \varphi(n))}$$
$$\varphi(n) = \frac{2\pi m}{M} + \varphi_0, \quad m = 0, 1, \ldots M-1 \tag{20}$$

where q is the symbol envelope, T_d is the symbol period, N is the number of bits, and φ_0 is the initial phase. $M = 2$ for binary coded signals, and $M = 4$ for Quaternary coded signals. The Barker code signal (B-PCS) and Frank code signal (F-PCS) are two common PCSs. Fig.3(b) presents a 13-bit B-PCS with $N = 13$, $M = 2$, $T = 2.6$ us, $\varphi_0 = 0$, and $f_c = 10$ MHz. Fig.3(c) presents a 16-bit F-PCS with $N = 16$, $M = 4$, $T = 3.2$ us, $\varphi_0 = 0$, and $f_c = 10$ MHz.

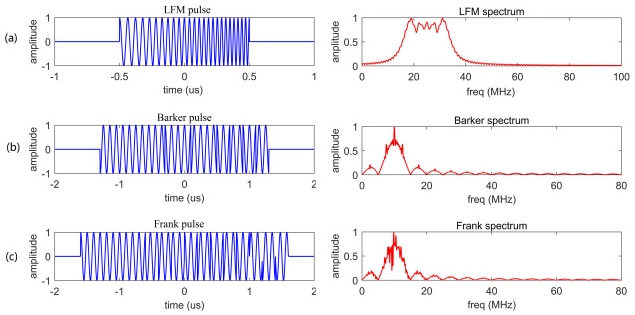

FIGURE 3. The waveforms and spectrum of pulse-compression signals: (a) LFM signal, (b) 13-bit B-PCS, (c) 16-bit F-PCS.

B. ATMOSPHERIC DUCT MODEL

The atmosphere refractive index usually varies with altitude and can be regrated as a layered structure. A modified version called modified refractivity M is introduced to take into account the effect of earth curvature by defined as

$$M(z) = \left[n(z) - 1 + \frac{z}{r_e}\right] \times 10^6, \tag{21}$$

where n is the refractive index, z is the altitude, and $r_e \approx$ 6371 km is earth's radius. In the marine environment, atmospheric anomalies often occur in relation to the inversions of atmospheric temperature and humidity. When the gradient $dM/dz < 0$ holds, the propagation direction of the electromagnetic wave is bent towards the earth, resulting in an abnormal propagation phenomenon.

Evaporation ducts are common in marine environments and have significant impacts on the long-distance radio wave propagation [28], [29]. The Paulus-Jeske (P-J) model provides a modified refractivity profile for evaporation duct [30]

$$M(z) = M_0 + C_0\left(z - h_d \ln\frac{z + Z_0}{Z_0}\right), \tag{22}$$

where M_0 is the base modified refractivity, $C_0 = 0.125$ M-unit/m is the linear slope of the refractivity, and $Z_0 = 1.5 \times 10^{-4}$ m is the roughness factor. When the height of evaporation h_d is set to zero, $M(z)$ is reduced to the modified refractivity of standard atmospheric. Fig.4(a) presents a modified refractivity profile for evaporation duct with $h_d = 40$ m.

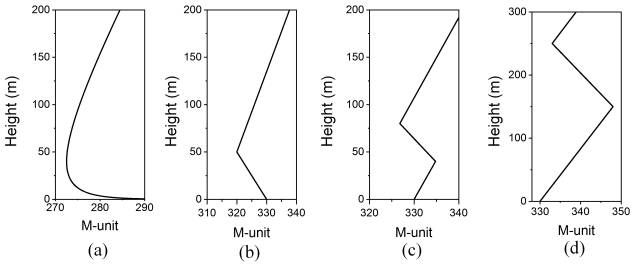

FIGURE 4. The M-profiles typical for (a) evaporation duct, (b) surface duct with ground-based layer, (c) surface duct with elevated layer, (d) elevated duct.

In addition, a piecewise-linear function is usually used to approximate the modified refractivity profiles of surface ducts and elevated ducts, which is expressed as

$$M(z) = M_0 + \begin{cases} C_1 z & z \le h_b \\ C_1 h_b - M_d \dfrac{z - h_b}{z_t} & h_b < z < h_t \\ C_1 h_b - M_d + C_2(z - h_b - z_t) & z \ge h_t, \end{cases} \tag{23}$$

where C_1 and C_2 are the slope coefficients of the base and top layers of the atmospheric duct, respectively, h_b and h_t are the base and top heights of the duct, respectively, z_t is the thickness of trapping layer, and M_d is the strength of duct. Fig.4(b)∼(d) present the refractivity profiles for (b) surface duct with ground-based layer, (c) surface duct with elevated layer, and (d) elevated duct, respectively.

C. EXAMPLES AND DISCUSSION

In this section, some examples are presented to validate the feasibility and validity of PE method for pulse-compression signal propagation and parameter estimation.

In the first example, to verify the correctness of the PE method in calculating the propagation of pulse compression signals, we compare the PE results with those of geometrical theory of diffraction (GTD) in a canonical single knife-edge scenario. The pulse considered here is a single LFM signal with a center frequency of 300 MHz, a pulse duration of 2 us and a bandwith of 40 MHz. The horizontal polarized transmitting antennas is placed at a height of 60 m, with an elevation of $-3°$ and a half power beamwidth of 7°. The height of the single knife-edge is 60 m. The horizontal distance between the knife-edge and the transmitting antenna is 600 m.

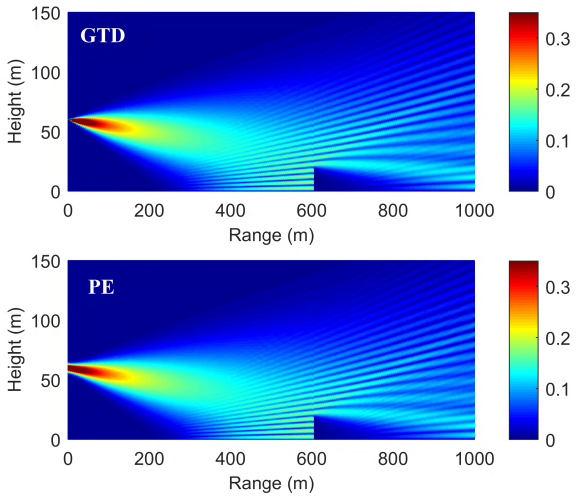

FIGURE 5. Electric field distribution corresponding to the center frequency calculated by PE method and GTD, respectively (unit:dBV/m).

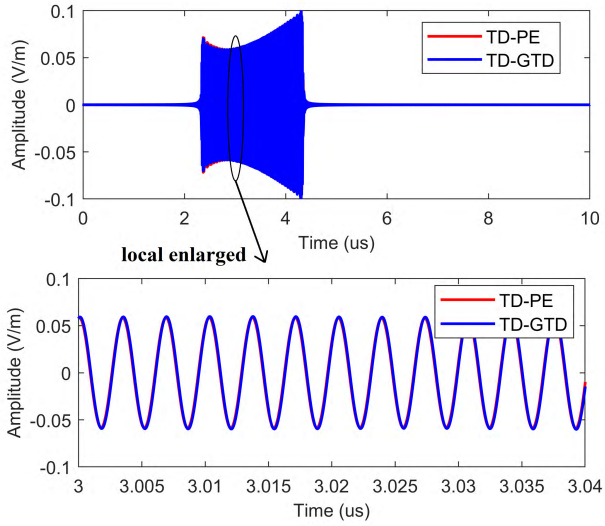

FIGURE 6. The received pulse at observation position (1000 m, 30 m) calculated by TD-PE method and TD-GTD, respectively.

Fig.5 presents the electric field distribution corresponding to the center frequency calculated by PE method and GTD, respectively. In Fig.5, the total field is a superposition of direct wave, ground reflection wave and diffraction wave generated by knife-edge. Obvious fringes appear at specific locations thanks to the interference phenomena of electromagnetic wave. The calculation results of these two methods show good consistency. Fig.6 shows the received pulses at observation position (1000 m, 30 m) calculated by the sliding window TD-PE method and TD-GTD, respectively. As shown, the results of the two methods are consistent.

In the second example, we discuss the propagation in the atmospheric duct environment. Fig.7 shows the electric field in dB calculated by PE method and the trajectories of electromagnetic wave propagation obtained from ray tracing method in different duct types. The corresponding M-profiles

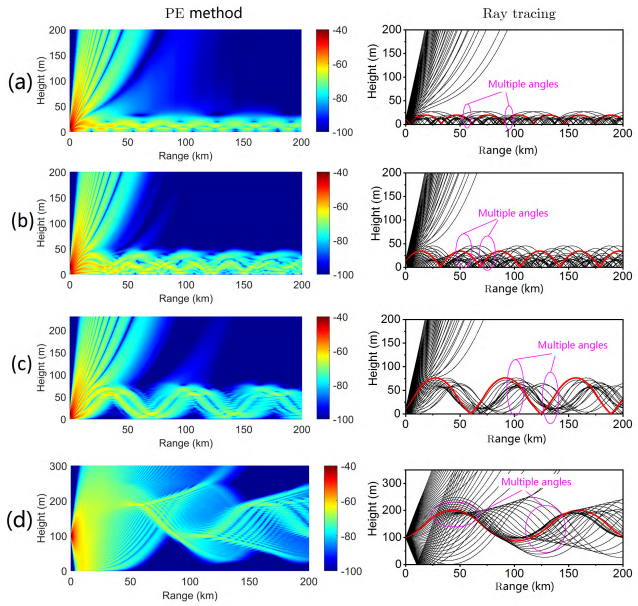

FIGURE 7. The simulation results obtained from PE method and ray tracing in different duct types: (a) Evaporation duct. (b) surface duct with ground-based layer. (c) surface duct with elevated layer. (d) Elevated duct. The simulation frequency is 10 GHz in PE method, and the corresponding M-profiles are presented in Fig.4.

TABLE 1. Parameters of transmitted radar signals.

Signals	f_c /GHz	T_d /us	T /us	B /MHz
LFM	10	0.02	0.2	40
13-bit B-PCS	5	0.02	0.26	50
16-bit F-PCS	3	0.02	0.32	50

are presented in Fig.4. The beamwidth of a horizontally polarized antenna with Gauss pattern is set to 0.9°. As shown in Fig.7, the PE results are consistent with those of ray tracing. To show the correctness of the time-delay estimation method, simulations with different signal types are presented, i.e. a LFM signal with carrier frequency 10 GHz, a 13-bit B-PCS with carrier frequency 5 GHz, and a 16-bit F-PCS with carrier frequency 3 GHz. The specific parameters are given in Table 1. In ray tracing, the effect of medium on the propagation velocity is considered via $v_c = c_0/Re(n_r(r, z))$, where $n_r(r, z) = n(r, z)+z/r_e$ denotes the modified refractive index. The trajectories of radio wave propagation between the transmitter and receiver are marked with red curves in Fig.7. Table 2 compares the propagation time-delays estimated by ray tracing (ΔT_{rt}) and PE method (ΔT_{pe}), respectively. As shown, the PE results are consistent with those of ray tracing, and the maximum differences between this two methods are no more than 2 ns, in other words, the maximum range differences not exceeding 0.6 m.

A example of flat ground with homogeneous atmospheric ($n = 1$) is presented to illustrate the performance of the presented DOA estimation method. The height of the transmitting antenna is 200 m and the observation height is fixed

TABLE 2. Time delays (ΔT) calculated via PE method and ray tracing method, respectively.

Duct types	Evaporation duct	Surface duct with ground-based layer	Surface duct with elevated layer	Elevated duct
Transmitter location /(km, m)	(0, 12)	(0, 15)	(0, 12)	(0, 100)
Receiver location /(km, m)	(200, 9.69)	(200, 33.24)	(200, 32.1)	(200, 105.13)
ΔT_{rt} /us	666.8517	666.8836	666.8876	666.8957
ΔT_{pe} (LFM) /us	666.8526	666.8850	666.8892	666.8971
ΔT_{pe} (B-PCS) /us	666.8529	666.8852	666.8893	666.8971
ΔT_{pe} (F-PCS) /us	666.8526	666.8852	666.8893	666.8971
maximum difference /ns	1.2	1.7	1.6	1.4

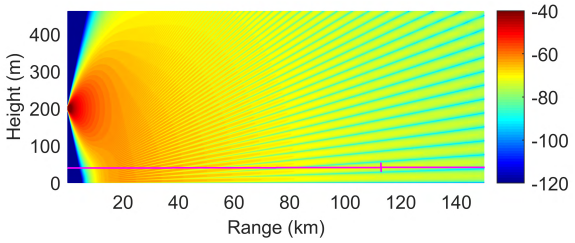

FIGURE 8. Electric field in dB calculated by PE with frequency 3 GHz and antenna beamwidth 0.9°.

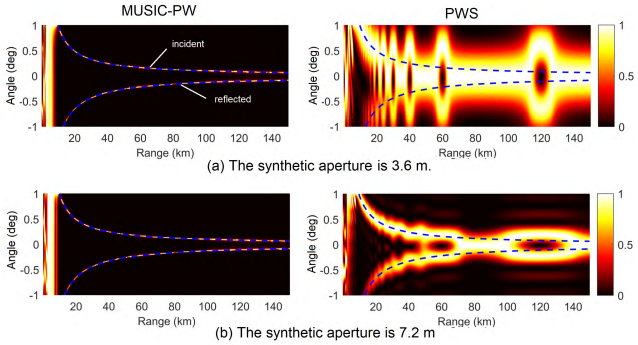

FIGURE 9. DOA estimations on a flat ground with homogeneous atmosphere using MUSIC-PW method and PWS method, respectively. The synthetic apertures are 3.6 m in (a) and 7.2 m in (b). The blue dashed lines denote the results obtained from the ray tracing.

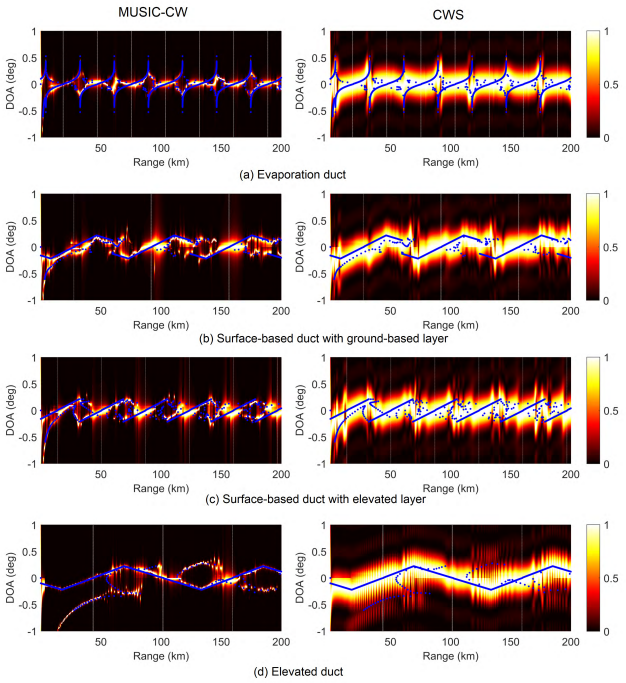

FIGURE 10. DOA estimations in different duct types: (a)Evaporation duct. (b)Surface duct with ground-based layer. (c)Surface duct with elevated layer. (d)Elevated duct. The blue dotted lines denote the results obtained from ray tracing.

at 30 m. The DOA here is defined as the grazing angle. Fig.8 shows the electric field calculated from PE. Apparently, there are two propagation paths, i.e. incident path and ground reflected path, forming a significant interference phenomenon. Because the propagation medium is uniform, the electromagnetic wave propagates along a straight line and reflects on the ground. Fig.9(a) and (b) present the angular power spectrum calculated by MUSIC-PW method (using (15)) and PWS method with synthetic apertures 3.6 m and 7.2 m, respectively. The amplitudes of the spectrum are normalized by the maximum power over the whole range. The blue dashed lines depict the results obtained from ray tracing. The MUSIC-PW results are in good agreement with those of ray tracing, as shown in Fig.9. In contrast, the MUSIC-PW method exhibits a better performance than PWS, although the resolution of the latter can be improved via enlarging the synthetic aperture.

Examples with atmospheric ducts are considered. The simulation scenarios are identical to those of Fig.7, where the M-profiles are presented in Fig.4. The simulation frequency is set to 5 GHz in PE, and the synthetic apertures are 7.2 m for both MUSIC-CW (using (13)) method and CWS method. For convenient comparisons, the observation positions are set to along the red curves depicted in Fig.7. Since multiple electromagnetic wave components arrive at the synthetic array in different directions, the situations considered here are more complicated than the previous one. The DOAs obtained from ray tracing are described as blue dotted lines in the figures. As shown in Fig.10, the results of MUSIC-CW and CWS are consistent with those of ray tracing on the whole. However, the former shows a higher resolution and distinguishes multiple angles effectively.

IV. EXPERIMENTS IN THE TROPOSPHERE

In the troposphere, atmospheric refraction and multipath phenomena are major environmental factors causing radar signal estimation errors. In particular, the random atmospheric ducts make it difficult for radar systems to accurately predict the

FIGURE 11. Experiment scenario. The ship-borne transmitter was located 12 m high above sea level and the receivers were installed on the land.

propagation path of electromagnetic waves, and measurement corrections are required to achieve a more reliable assessment. On the other hand, despite the adverse effects, the trapping effects of atmospheric ducts make part of the electromagnetic wave propagate to a far distance with a small attenuation and implement radars' over-the-horizon detection.

PE method was applied to predict the propagation of radar signals in a typical sea-to-land scenario in the eastern coastal areas of China, as shown in Fig.11. Since the evaporation ducts have the highest probability of occurrence among all kinds of ducts in the marine environment, the sensitivity of pulse-compression signal to evaporation ducts is analyzed, including the waveform distortion, time delay, and DOA (defined as the grazing angle).

The ship-borne transmitter marked with purple square in Fig.11 was located 12 m high above sea level. The main lobe of the transmitting antenna was along the purple arrow. The positions of the receivers were marked with red squares in the map. The altitude of R $\times$ 1 was 21 m and that of R $\times$ 2 was 380 m. The ground distances from the transmitter to R $\times$ 1 and R $\times$ 2 were 134.7 km and 139.7 km, respectively. The SNR of the receiver was 15 dB. A LFM signal emitted by an antenna with a 0.9° Gaussian beam pattern has a center frequency of 3 GHz, pulse width 1.6 us, and bandwidth 30 MHz. The pulse wavefrom and spectrum are shown in Fig.12(a). The time-domain observation window in TD-PE was set to 8 us. Accordingly, the number of frequency points for PE calculation was $N_f' = 240$. The refractivity was assumed to be uniformly distributed along the horizontal direction in this experiment, yet it should be noted that the presented method is applicable to arbitrarily varying refractivity.

In practice, because of the multipath phenomenon, there are often multiple signals arriving at the receiver at different time. If the relative delays between each signal are far less than a symbol period, the multipath effect will not cause inter-symbol interference. On the contrary, if the relative delays are not negligible compared with a symbol period, then the multi-channel signals overlap with each other, resulting in frequency selective fading.

Fig.12(b)∼(d) present the received pulses at R $\times$ 1 and their corresponding spectrum at different evaporation duct heights (EDHs). From the results we can see that, at R $\times$ 1, the waveforms of the received pulses are basically the same as that of the transmitted pulse except for amplitude due to the attenuation. Fig.13(b)∼(d) present the received pulses and their corresponding spectrum at R$\times$2. Fig.13(b) shows that no obvious distortion in waveform occurs when EDH was 20 m. However, when EDH increases to 50 m, the received signal appears frequency selective fading due to the multi-path effect, and its waveform has a serious distortion. However, considering the fact that EDH is usually less than 40 m in practice, the probability of this happening is low. To quantify the signal distortion, the root-mean-square (RMS) difference

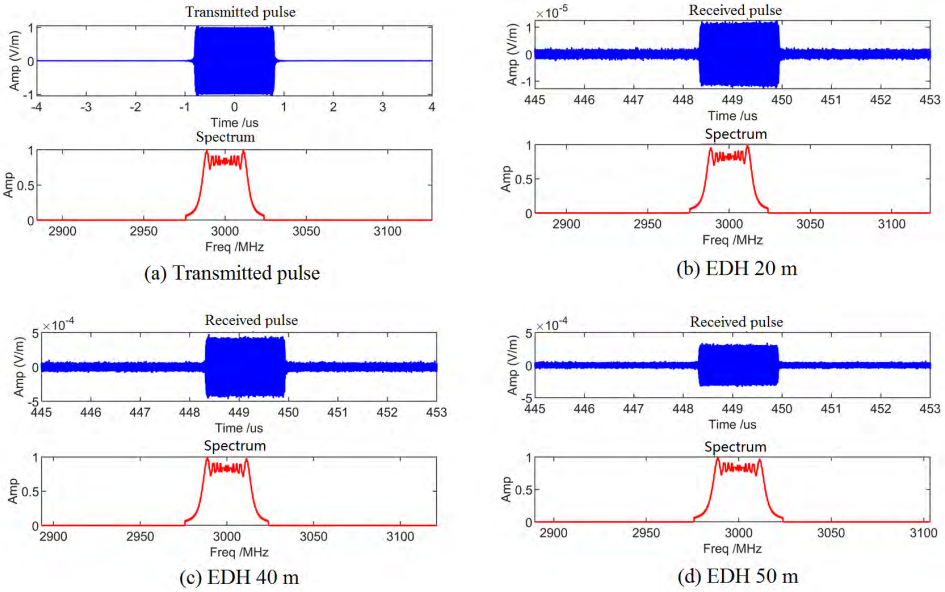

FIGURE 12. (a) The transmitted pulse and its spectrum. (b)∼(d) The received pluses at R $\times$ 1 at different evaporation duct heights.

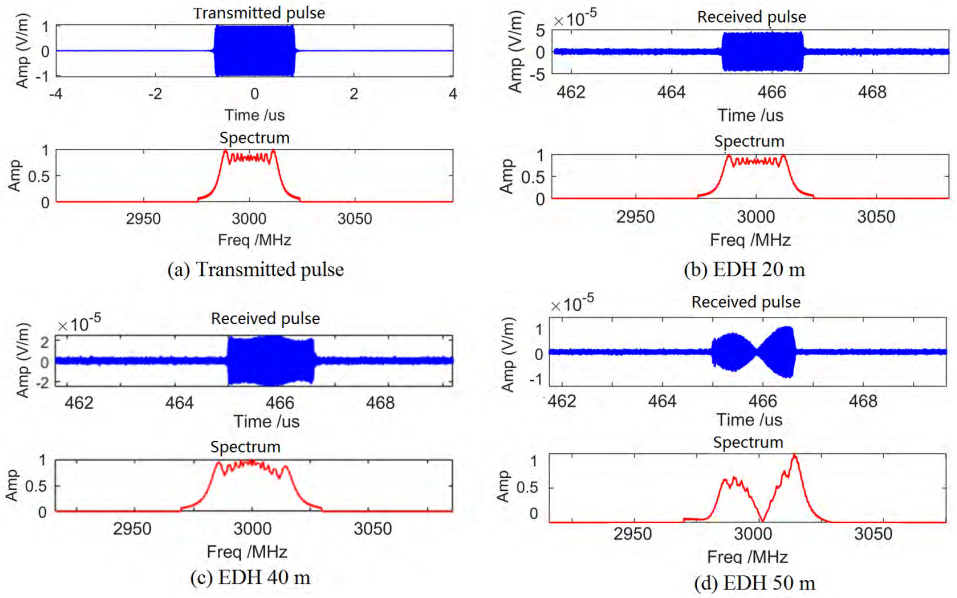

FIGURE 13. (a) The transmitted pulse and its spectrum. (b)∼(d) The received pluses at R × 2 at different evaporation duct heights.

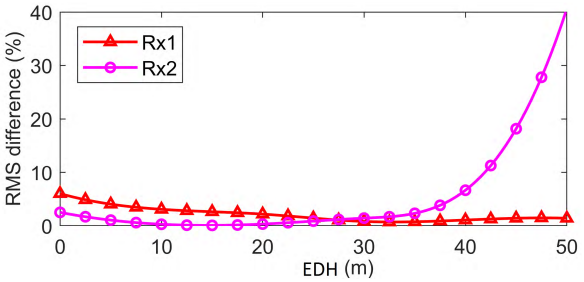

FIGURE 14. The RMS difference of normalized spectrum between the transmitted and received signals.

between the normalized spectrum of the transmitted and received signals is introduced, which is expressed as

$$\eta = \sqrt{\frac{\sum_{n=k_1}^{k_2} [f_t(n) - f_r(n)]^2}{N_f'}}, \tag{24}$$

where k_1 and k_2 are the serial numbers of the band lower frequency and band high frequency, respectively, f_t and f_r are the transmitted and received signal spectrum, respectively, and N_f' is the sampling number in the frequency band. As shown in Fig.14, for both R × 1 and R × 2, $\eta < 7\%$ when the evaporation duct height is less than 40 m, which indicates that the pulse waveform is not sensitive to the evaporation duct.

Different radar signals were simulated to estimate the time delay at receivers. The signals have the same pulse width 1.6 us, and the carrier frequencies of the 13-bit B-PCS and 16-bit F-PCS are the same as the central frequency of LFM, i,e. 3 GHz, with bandwidth of 8 MHz and 10 MHz, respectively. The results are presented in Fig.15. With the increase of EDH, more electromagnetic wave energy was trapped in

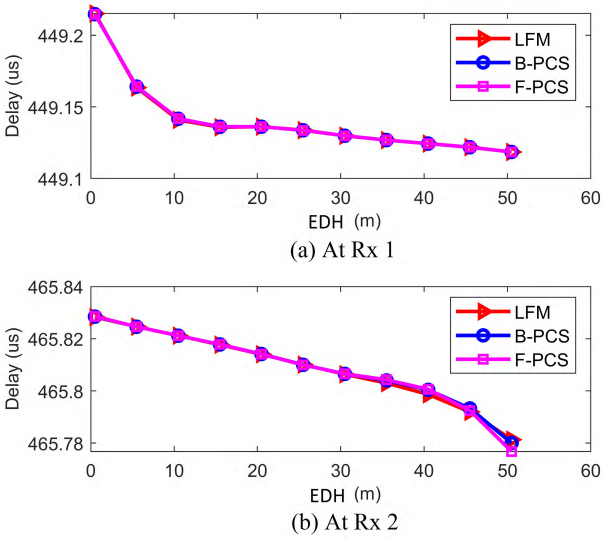

FIGURE 15. Delay estimation results at the receivers using different radar signals with the same pulse width.

the duct layer. The simulation results of the three radar signals are consistent, which illustrates that the signal delay is independent of the signal type. It also shows that the presented method has the same accuracy in calculating of these signals. In addition, the delays decrease with EDH, which indicates that the evaporation ducts force electromagnetic waves to propagate along a shorter path.

Fig.16 presents the DOA estimation results at the receivers in different radar bands, where the synthetic aperture was set to 3.6 m. As shown, all DOAs are less than 1°. When EDHs exceed a certain threshold (20 m for R × 1, and 10 m for R × 2), the DOAs in different frequency bands are close to

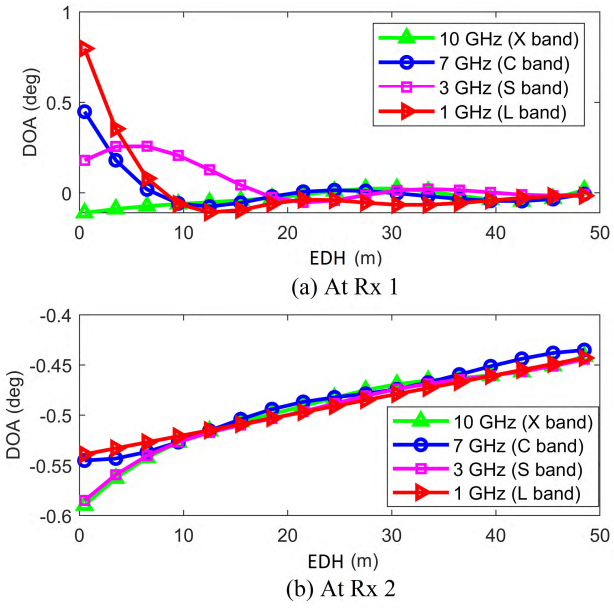

FIGURE 16. DOA estimation at receiver R × 1 and R × 2 in different radar frequency bands.

each other. The DOAs of R × 1 tend to be 0 degree when EDH is larger than 20 m, and the absolute value of DOAs for R × 2 also decreases with EDH. The results obtained are consistent with the fact that evaporative ducts force the electromagnetic waves propagating along the earth's surface.

V. CONCLUSION

In this paper, a time-domain version of PE is applied to model the propagation of pulse-compression signals in the troposphere, taking into account the abnormal atmospheric. A sliding window method which requires a small observation window is used to reduce the computational loads for a long-range case. Considering the autocorrelation of the signals, the propagation delay is obtained by searching the peak of the correlation function between the received signal and a known reference signal. This method has proved to be particularly suitable for pulse compression signals. A MUSIC algorithm is introduced to estimate the DOAs of the signals, where the covariance matrix is constructed via the array fields obtained from PE and the curvature of the wavefronts is considered in the array steering vector. Simulation results show that this method has a higher resolution and requires a smaller synthetic aperture compared with the traditional spectral methods. Finally, simulation experiments in a typical sea-to-land scenario are presented to analyze the sensitivity of pulse-compression signals to the evaporation ducts. The experimental results show that, the waveform distortion caused by evaporation ducts is not obvious, while the propagation delay and DOA decrease with the duct height. In this paper, the feasibility of PE estimating signal parameters in the troposphere has been verified, and it has the potential for further improvements to construct a more comprehensive model by taking the effects of sea clutter, rainfall, fog and clouds into consideration.

REFERENCES

[1] A. Danklmayer, J. Förster, V. Fabbro, G. Biegel, T. Brehm, P. Colditz, L. Castanet, and Y. Hurtaud, "Radar propagation experiment in the north sea: The Sylt campaign," *IEEE Trans. Geosci. Remote Sens.*, vol. 56, no. 2, pp. 835–846, Feb. 2018.
[2] M. A. Rico-Ramirez and I. D. Cluckie, "Classification of ground clutter and anomalous propagation using dual-polarization weather radar," *IEEE Trans. Geosci. Remote Sens.*, vol. 46, no. 7, pp. 1892–1904, Jul. 2008.
[3] Q. Wang, R. J. Burkholder, C. Yardim, L. Xu, J. Pozderac, A. Christman, H. J. S. Fernando, D. P. Alappattu, and Q. Wang, "Range and height measurement of X-band EM propagation in the marine atmospheric boundary layer," *IEEE Trans. Antennas Propag.*, vol. 67, no. 4, pp. 2063–2073, Apr. 2019.
[4] L. Sevgi, "Synthetic radar-signal environment: Computer generation of signal, noise, and clutter," *IEEE Antennas Propag. Mag.*, vol. 49, no. 5, pp. 192–198, Oct. 2007.
[5] J. P. Reilly and G. D. Dockery, "Influence of evaporation ducts on radar sea return," *IEE Proc. F Radar Signal Process.*, vol. 137, no. 2, pp. 80–88, Apr. 1990.
[6] L. Zhou, X. Xi, J. Liu, and N. Yu, "LF ground-wave propagation over irregular terrain," *IEEE Trans. Antennas Propag.*, vol. 59, no. 4, pp. 1254–1260, Apr. 2011.
[7] J. J. Simpson and A. Taflove, "Three-dimensional FDTD modeling of impulse ELF propagation about the earth-sphere," *IEEE Trans. Antennas Propag.*, vol. 52, no. 2, pp. 443–451, Feb. 2004.
[8] J. T. Johnson, R. T. Shin, J. C. Eidson, L. Tsang, and J. A. Kong, "A method of moments model for VHF propagation," *IEEE Trans. Antennas Propag.*, vol. 45, no. 1, pp. 115–125, Jan. 1997.
[9] M. Levy, *Parabolic Equation Methods for Electromagnetic Wave Propagation*. London, U.K.:, 2000.
[10] G. D. Dockery, "Modeling electromagnetic wave propagation in the troposphere using the parabolic equation," *IEEE Trans. Antennas Propag.*, vol. AP-36, no. 10, pp. 1464–1470, Oct. 1988.
[11] R. Akbarpour and A. R. Webster, "Ray-tracing and parabolic equation methods in the modeling of a tropospheric microwave link," *IEEE Trans. Antennas Propag.*, vol. 53, no. 11, pp. 3785–3791, Nov. 2005.
[12] G. Apaydin and L. Sevgi, "The split-step-fourier and finite-element-based parabolic-equation propagation-prediction tools: Canonical tests, systematic comparisons, and calibration," *IEEE Antennas Propag. Mag.*, vol. 52, no. 3, pp. 66–79, Jun. 2010.
[13] A. E. Barrios, "A terrain parabolic equation model for propagation in the troposphere," *IEEE Trans. Antennas Propag.*, vol. 42, no. 1, pp. 90–98, Jan. 1994.
[14] V. A. Permyakov, M. S. Mikhailov, and E. S. Malevich, "Analysis of propagation of electromagnetic waves in difficult conditions by the parabolic equation method," *IEEE Trans. Antennas Propag.*, vol. 67, no. 4, pp. 2167–2175, Apr. 2019.
[15] M. S. Mikhailov, E. S. Malevich, and V. A. Permyakov, "Modeling of radio-wave propagation in forest by the method of parabolic equation," *Int. J. Eng. Technol.*, vol. 7, nos. 2–23, pp. 111–113, 2018.
[16] J. Ramakrishna, "Path loss predictions in the presence of buildings on flat terrain: A 3-D vector parabolic equation approach," *IEEE Trans. Antennas Propag.*, vol. 51, no. 8, pp. 1716–1728, Aug. 2003.
[17] N. Sheng, C. Liao, W. Lin, Q. Zhang, and R. Bai, "Modeling of millimeter-wave propagation in rain based on parabolic equation method," *IEEE Antennas Wireless Propag. Lett.*, vol. 13, pp. 3–6, Dec. 2013.
[18] R. H. Hardin, "Applications of the split-step Fourier method to the numerical solution of nonlinear and variable coefficient wave equations," *SIAM Rev.*, vol. 15, no. 2, pp. 423–429, 1973.
[19] J. Feng, L. Zhou, X. Xu, and C. Liao, "A hybrid TDPE/FDTD method for site-specific modeling of O2I radio wave propagation," *IEEE Antennas Wireless Propag. Lett.*, vol. 17, no. 9, pp. 1652–1655, 2018.
[20] J. Shi, G. Hu, B. Zong, and M. Chen, "DOA estimation using multipath echo power for MIMO radar in low-grazing angle," *IEEE Sensors J.*, vol. 16, no. 15, pp. 6087–6094, Aug. 2016.
[21] Y. Liu, H. Liu, X.-G. Xia, L. Zhang, and B. Jiu, "Projection techniques for altitude estimation over complex multipath condition-based VHF radar," *IEEE J. Sel. Topics Appl. Earth Observ. Remote Sens.*, vol. 11, no. 7, pp. 2362–2375, Jul. 2018.

[22] R. O. Schmidt, "Multiple emitter location and signal parameter estimation," *IEEE Trans. Antennas Propag.*, vol. AP-34, no. 3, pp. 276–280, Mar. 1986.
[23] A. E. Barrios and W. L. Patterson, "Advanced propagation model (APM) Ver. 1.3.1 computer software configuration item (CSCI) documents," Space Naval Warfare Syst. Center, San Diego, CA, USA, Tech. Rep. 3145, Aug. 2002.
[24] A. Karimian, C. Yardim, P. Gerstoft, W. S. Hodgkiss, and A. E. Barrios, "Multiple grazing angle sea clutter modeling," *IEEE Trans. Antennas Propag.*, vol. 60, no. 9, pp. 4408–4417, Sep. 2012.
[25] D. Dockery and J. R. Kuttler, "An improved impedance-boundary algorithm for Fourier split-step solutions of the parabolic wave equation," *IEEE Trans. Antennas Propag.*, vol. 44, no. 12, pp. 1592–1599, Dec. 1996.
[26] D. J. Donohue and J. R. Kuttler, "Propagation modeling over terrain using the parabolic wave equation," *IEEE Trans. Antennas Propag.*, vol. 48, no. 2, pp. 260–277, Feb. 2000.
[27] S. U. Pillai and B. H. Kwon, "Forward/backward spatial smoothing techniques for coherent signal identification," *IEEE Trans. Acoust., Speech Signal Process.*, vol. 37, no. 1, pp. 8–15, Jan. 1989.
[28] J. Pozderac, J. Johnson, C. Yardim, C. Merrill, T. de Paolo, E. Terrill, F. Ryan, and P. Frederickson, "*X*-band beacon-receiver array evaporation duct height estimation," *IEEE Trans. Antennas Propag.*, vol. 66, no. 5, pp. 2545–2556, May 2018.
[29] R. A. Paulus, "Practical application of an evaporation duct model," *Radio Sci.*, vol. 20, no. 4, pp. 887–896, Jul./Aug. 1985.
[30] L. T. Rogers, C. P. Hattan, and J. K. Stapleton, "Estimating evaporation duct heights from radar sea echo," *Radio Sci.*, vol. 35, no. 4, pp. 955–966, 2000.

DONGMIN ZHANG was born in Hunan, China, in 1990. He received the B.E. degree in electronic information science and technology from Southwest Jiaotong University, Chengdu, China, in July 2015, where he is currently pursuing the Ph.D. degree in electromagnetic field and microwave technology. His research interests include computational electromagnetics and electromagnetic wave propagation.

CHENG LIAO received the B.S. and M.S. degrees in optics and the Ph.D. degree in electromagnetic field and microwave technology from the Chengdu University of Electronic Science and Technology, Chengdu, China, in 1986, 1989, and 1995, respectively. He is currently a Professor and the Director of the Institute of Electromagnetic Field and Microwave Technology, Southwest Jiaotong University. His major research interests include antenna theory and design, computational electromagnetics, and electromagnetic scattering.

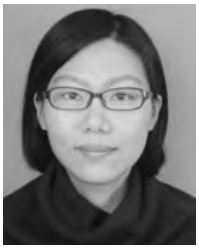

JU FENG received the Ph.D. degree in electromagnetic field and microwave technology from Southwest Jiaotong University, Chengdu, China, in 2014. She is currently an Associate Professor with the Institute of Electromagnetic Field and Microwave Technology, Southwest Jiaotong University. Her major research interests include antenna theory and design, computational electromagnetics, and electromagnetic wave propagation.

XIAOCHUAN DENG was born in Sichuan, China, in 1990. He received the B.E. degree in electromagnetic wave propagation and antenna from the Chengdu University of Electronic Science and Technology, Chengdu, China, in July 2014. He is currently pursuing the Ph.D. degree in electromagnetic field and microwave technology with Southwest Jiaotong University. His research interests include computational electromagnetics and electromagnetic wave propagation.